

Research Papers

Determination of internal temperature of EV battery modules via electrochemical impedance spectroscopy (EIS) and distribution of relaxation times (DRT)

M. Kemeny ^{a,*}, P. Ondrejka ^a, D. Sismisova ^b, M. Mikolasek ^a

^a Institute of Electronics and Photonics, Slovak University of Technology in Bratislava, Ilkovicova 3, 812 19 Bratislava, Slovakia

^b ZTS – Výskum a Vyvoj, a.s., Lieskovec 598/75, 018 41 Dubnica nad Vahom, Slovakia



ARTICLE INFO

Keywords:

Li-ion batteries
Electric vehicles
Internal temperature
Electrochemical impedance spectroscopy
Distribution of relaxation times

ABSTRACT

This study presents an analysis of the suitability of electrochemical impedance spectroscopy (EIS) features, obtained through equivalent circuit model (ECM) fitting and distribution of relaxation times (DRT), for determining the internal temperature of an electric vehicle (EV) battery module in both EV and 2nd life applications. Temperature-dependent ECM and DRT features were identified, and their ability to accurately determine the internal temperature of the module was evaluated. The analysis was conducted over a temperature range of 0 °C to 50 °C in 10 °C increments, and for states of charge (SOCs) ranging from 10 % to 90 % in 10 % increments, covering and exceeding the optimal temperature and SOC operating conditions for the studied 24 kWh Nissan Leaf module. The findings suggest that, among the ECM and DRT features, the DRT peak corresponding to the highest frequencies is the most suitable feature for determining the internal temperature of EV battery modules.

1. Introduction

The development of battery management systems (BMSs) is crucial for further electrification across many industries, with the goal to achieve carbon neutrality [1,2]. The pivot topics are the wider integration of electric vehicles (EVs) in public transport and the broader use of renewable sources of energy [3,4]. Since 1991, when the first commercial Li-ion battery hit the shelves [5], the development of Li-ion batteries has led to astonishing results, allowing an extensive rise in the EV industry [6,7] and in stationary energy systems and 2nd life applications. Despite the success of modern battery technologies, some safety concerns remain to this day [8,9]. Needless to say, the greatest safety risk arising from the use of current batteries in both EV and 2nd life applications is the possibility of malfunction and thermal runaways, leading to fires or explosions [10–12]. Moreover, when it comes to EV battery modules, it is essential to maintain optimal thermal conditions in order to suppress various temperature-induced degradation mechanisms, which, aside from safety risks, can easily decrease the longevity of the battery modules [13,14]. Considering this, it is of vital importance to monitor the internal temperature of battery modules to address temperature changes, or in extreme scenarios, provide early warning of thermal runaways [15,16]. Unfortunately, integrating temperature

sensors inside battery cells is highly problematic. Therefore, the temperature of the battery is commonly assessed by measuring the surface temperature of the battery casing [17,18]. Given the thermal capacity and conductivity of various polymers and metals used in cell and module casings, accurately estimating the real battery temperature based on the surface temperature measurements may be insufficient. To address these issues, it is desirable to search for in-operando characterisation approaches that enable to study temperature-dependent features of Li-ion batteries, where monitoring changes in these features would enable to determine the internal temperature of the battery [19,20]. One of the promising candidates for such purposes is impedance measurement in the frequency domain, known as electrochemical impedance spectroscopy (EIS) [21,22], or in the time domain, by means of current pulse responses measurements [23,24]. This work provides an analysis of the suitability of EIS features obtained via equivalent electric circuit fitting and distribution of relaxation times (DRT) for determining the internal temperature of used EV battery modules. Moreover, the applicability of using such features in real-world applications is discussed.

* Corresponding author.

E-mail address: martin.kemeny@stuba.sk (M. Kemeny).

2. Methodology

2.1. Electrochemical impedance spectroscopy

One of the most dominant advanced techniques used to study the properties of various electrochemical systems, such as batteries, is electrochemical impedance spectroscopy [25,26]. This technique allows the study of a wide range of battery features, such as an increase in ohmic resistance, changes in the solid electrolyte interface (SEI) layer, charge-transfer properties, and the diffusion of lithium ions (D_{Li^+}) [27,28]. The most common representation of EIS data is in the form of Nyquist plots. While these plots provide a good visual representation of the EIS data, it is usually necessary to parametrise these datasets using equivalent circuit models (ECMs) to numerically differentiate the contributions of individual electrochemical or dynamic processes [29]. Finding the correct ECM for a given system is often challenging since Nyquist plots can consist of several highly overlapping depressed semicircles, which cannot be reliably distinguished from each other solely by visual analysis. Hence, it requires some additional analysis and/or a good understanding of the studied system [30]. When the correct ECM is established, EIS data can be fitted by the circuit, resulting in parametrisation of the battery by individual ECM elements [31]. The changes in values of individual ECM elements can indicate various changes in the battery, such as the thickening of the SEI layer or decreasing charge-transfer properties of the cell. Moreover, Li-ion batteries are complex electrochemical systems in which several processes take place, each with its own temperature dynamic. Hence, EIS data fitting can also be used to analyse the temperature dependency of these ECM elements [32,33].

2.2. Distribution of relaxation times

In contrast to EIS data fitting via ECM, the distribution of relaxation times provides a model-free approach for the interpretation of EIS data [34,35]. Unlike ECM fitting, which uses a finite number of components to describe the studied system, DRT calculations assume that the system can be described by an infinite number of in-series connected $R||C$ elements [36]. These calculations enable the transformation of EIS data from the frequency-domain to the time-domain, resulting in several recognizable peaks, each representative of a single electrochemical process. Hence, DRT enables to distinguish the number of dominant electrochemical processes, with each of these processes manifesting in a different time-domain range [37]. This is particularly useful when Nyquist plots consist of several highly overlapping depressed semicircles, making the construction of a suitable ECM without specific assumptions is problematic [38]. By deconvoluting the studied system, DRT helps to identify the most suitable ECM and also provides time-constant parameters for its capacitive components (C , CPE), enabling more accurate fitting results. This DRT approach also allows the study of the influence of temperature or SOC on the dominant processes, where changes of these operating conditions can manifest as changes in the magnitude and/or positions of individual DRT peaks [39].

There are several approaches how to calculate DRT [40–42]. For this study, it was decided to use the universally applicable standard Tikhonov regularization, which was extensively discussed by Gavril'yuk et al. [43,44]. Arguably, the most significant challenge in DRT calculation is the determination of the correct regularization parameter λ . As it was discussed by Schlieter et al. [45], an excessively high λ leads to underinterpretation of the system, whereas too small λ results in overinterpretation. Therefore, in order to describe the system in the best possible manner, it is crucial to select λ as small as possible while avoiding too low λ values which would lead to insufficient filtering, resulting in the impedance data superimposed with noise.

3. Experimental

This experiment was designed to investigate the influence of the internal temperature (T_{INT}) of EV battery modules on individual ECM and DRT features, aiming to identify the most suitable EIS-based features for determining T_{INT} in real-world EV and 2nd life applications. For this purpose, a used 24 kWh Nissan Leaf module (2S2P) was studied, with one parallel sub-module (2S1P) used for EIS measurements. The state of health of the module was 85 %. These batteries contain $LiMn_2O_4$ with $LiNiO_2$ as the cathode and graphite as the anode. Their nominal capacity is 66.2 Ah/24kWh at a 0.3C rate. Aside from their commercial success in EV applications, the 2nd life potential of these battery modules was extensively studied and discussed by Gao et al. [46]. Their work clearly recognized the necessity of maintaining optimal temperature conditions for safe and long-lasting use of such modules in 2nd life applications.

The first step after disassembling the EV module from the battery pack was its conditioning via 10 charge/discharge cycles (C/2 CCCV charging up to 4.2 V and C/C CC discharging to 2.5 V) at 25 °C (± 0.5 °C fluctuation) in a temperature-controlled laboratory. This cycling procedure was done by a battery charge/discharge tester (ZKETech EBC-A40L, China). Subsequently, the module was discharged to SOC 50 % and allowed to relax for 24 h. After the relaxation, EIS measurements were conducted 10 times, with 1 h of relaxation between the measurements. The aim for these measurements was to obtain the data for the correct determination of the regularization parameter for DRT. All impedance measurements were carried out in galvanostatic fashion (frequency range 1 kHz – 10 mHz; AC current 3.5 A rms; 12 points per decade) using a potentiostat-galvanostat (GAMRY Interface 5000P, USA).

Subsequently, the module was placed inside a climate chamber (LIB TH-50, vol. 50 L, China) for the second analysis. The aim of this step was to determine the time required for the internal temperature of the module to reach the set temperature of the chamber. The chamber temperature was raised to 50 °C with a slope of 2 °C per minute. Once the chamber reached the set temperature, a series of 20 consecutive EIS measurements was conducted at 30-min intervals. The module was then allowed to relax at ambient temperature of the laboratory for 24 h, and the analysis was repeated at 0 °C. For each temperature, the EIS data were plotted together as Nyquist plots, and their alignment was examined. T_{INT} was considered stabilised at the desired temperature when three consecutive Nyquist plots overlapped.

Following these initial investigations, the main experiment was conducted. The optimal working conditions for these modules for their 2nd life use are between 15 °C and 25 °C and between SOC 90 % and 10 % [46]. Based on this, the temperature dependence of EIS and DRT features was studied and evaluated for temperatures ranging from 50 °C to 0 °C (in 10 °C increments), and for the state of charge ranging from SOC 90 % to 10 % (in 10 % increments). The study was conducted as follows: I. The module was conditioned through 3 charge/discharge cycles, followed by a single charging step (the same cyclic parameters as for the initial conditioning) at 25 °C to establish SOC 100 %. II. The module was then placed in the climate chamber, and the temperature was set to the desired value for a given analytical cycle. III. Once the set temperature was reached, the module was allowed to relax for 5 h to ensure sufficient and even heating and cooling (discussed in more detail in Section 4.2). After this relaxation, the temperature inside the climate chamber and the surface temperature of the module were considered equal to T_{INT} . IV. The module was then discharged to desired SOC using a C/20 constant current and relaxed for 1 h prior to EIS measurements. Discharging at such a low current was not expected to have a significant influence on T_{INT} , while the subsequent relaxation ensured that any possible temperature changes were suppressed, stabilizing T_{INT} at the desired temperature. V. After the SOC was set and the module was relaxed, EIS measurements were conducted. VI. The process of discharging to the remaining SOC steps, followed by relaxation periods and EIS

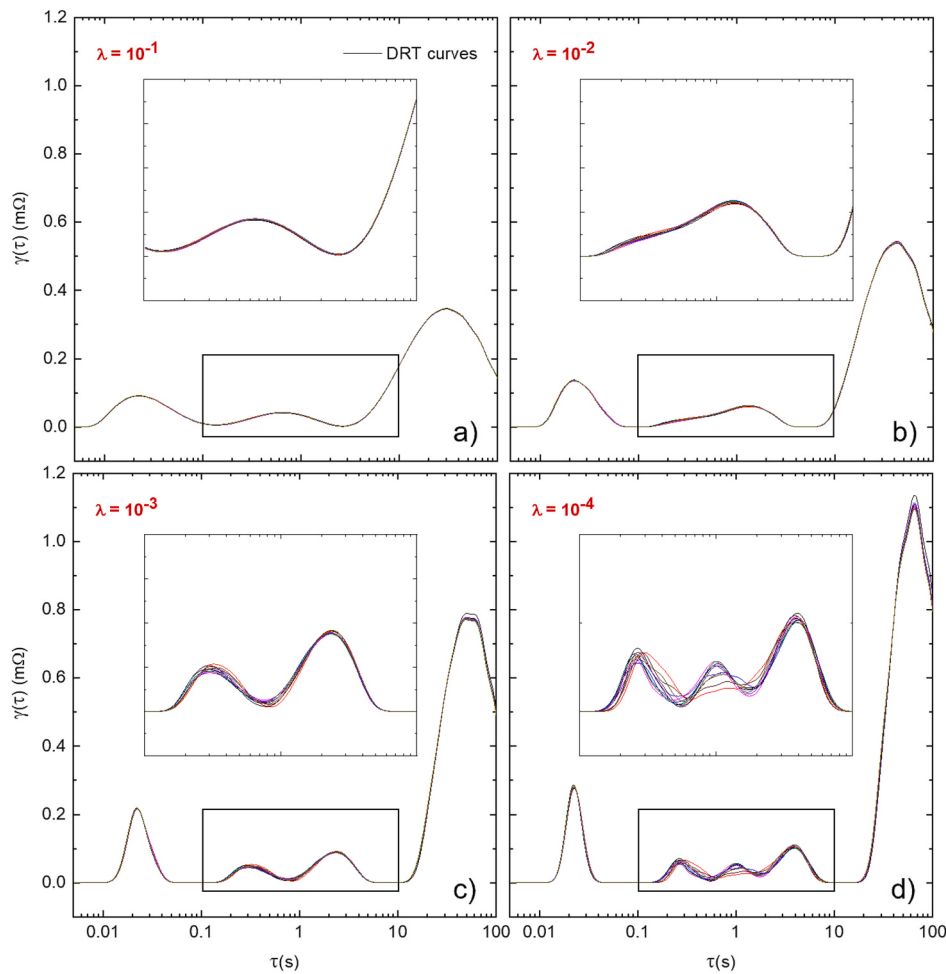


Fig. 1. DRT curves constructed with various regularization parameters: (a) $\lambda = 10^{-1}$, (b) $\lambda = 10^{-2}$, (c) $\lambda = 10^{-3}$, and (d) $\lambda = 10^{-4}$.

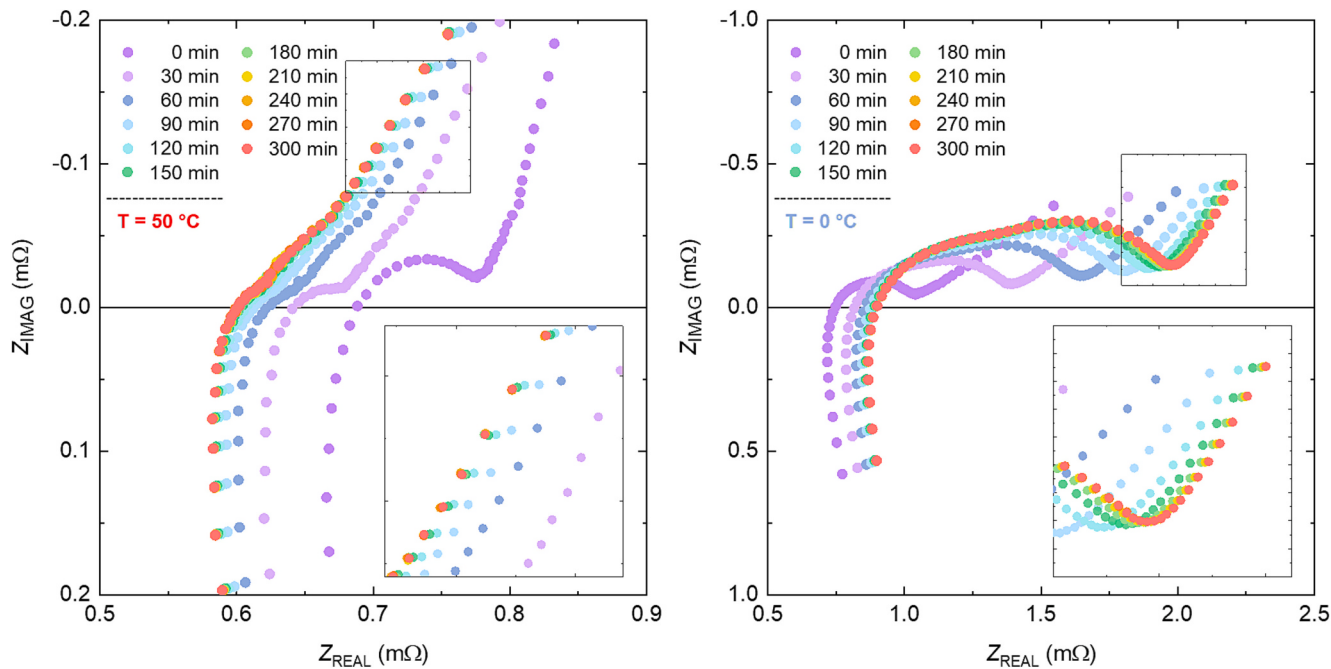


Fig. 2. Series of consecutive EIS measurements conducted at 30-min intervals at (a) 50 °C and (b) 0 °C for determination of time requirements for T_{INT} stabilisation.

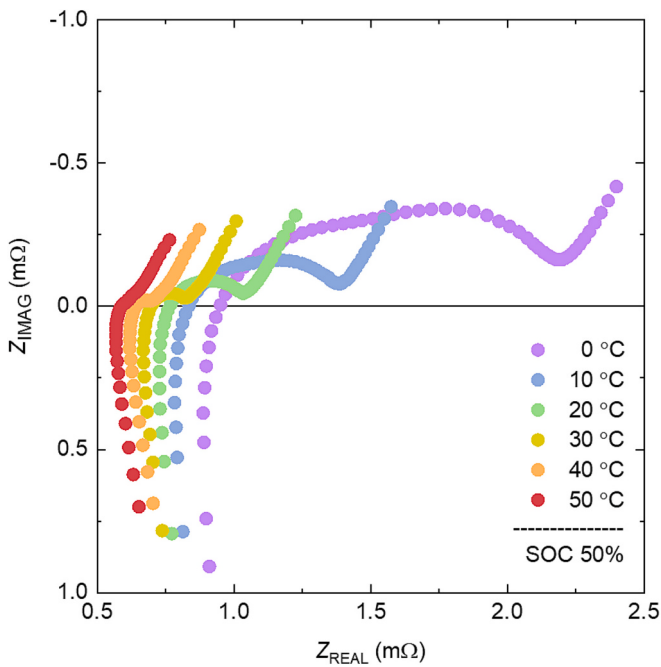


Fig. 3. Nyquist plots for various temperatures at SOC 50 %.

measurements, was repeated until EIS at SOC 10 % was measured. VII. The module was then removed from the climate chamber, allowed to relax for 24 h, and the entire process was repeated from the first step for all desired temperatures.

4. Results and discussion

4.1. Regularization parameter for standard Tikhonov regularization

DRT was calculated using standard Tikhonov regularization, where it is of vital importance to determine the correct regularization parameter. An excessively high regularization parameter λ leads to an under-interpretation of the system, whereas too small λ results in over-interpretation. Therefore, to describe the system in the best possible manner, it is necessary to select the smallest suitable λ , while avoiding values that are too low, as they would lead to insufficient filtering, causing impedance data to be undesirably superimposed by noise. The most suitable λ can be identified by comparing several DRT plots constructed from repetitive EIS measurements, where excessively small λ would result in notable variances between the DRT curves [45].

In order to find the most suitable λ for the studied system, the EIS measurements were repeated 10 times at SOC 50 % at 25 °C, while the module was resting for 1 h between the measurements. Prior to these measurements, the module had rested for 24 h, and hence it is expected that the module has fully reached its equilibrium state. The DRT curves were calculated using λ values of 10^{-1} , 10^{-2} , 10^{-3} , and 10^{-4} . The resulting DRT curves are shown in Fig. 1. As it can be seen, DRT curves calculated using $\lambda = 10^{-1}$ result in three recognizable individual features, while using $\lambda = 10^{-2}$ results in four features, two of which are merging into one central peak. $\lambda = 10^{-3}$ leads to four distinct DRT peaks,

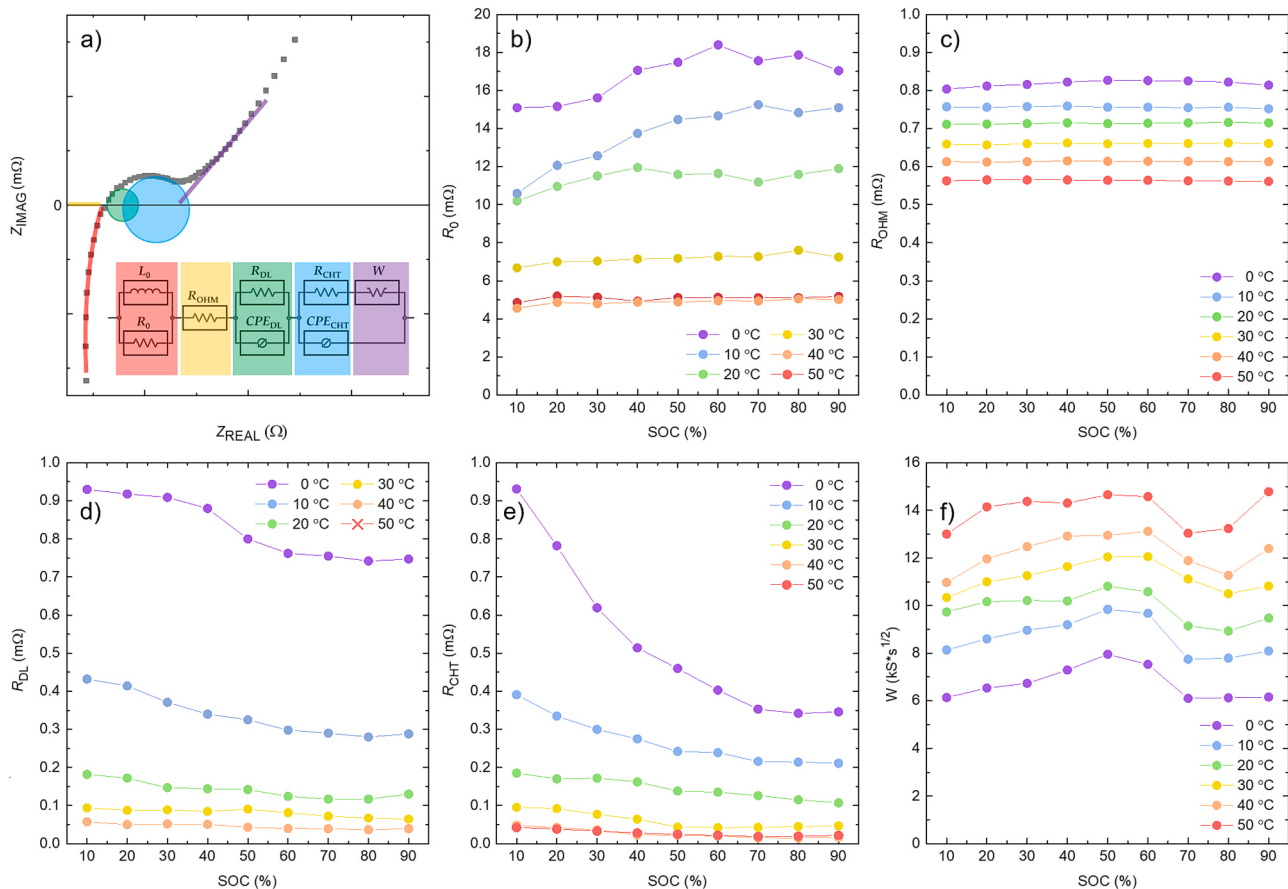


Fig. 4. (a) Visual division of a Nyquist plot into individual distinguishable features with according ECM in the plot inset; the results of the EIS data fitting: (b) R_0 , (c) R_{OHM} , (d) R_{DL} , (e) R_{CHT} , and (f) Warburg element.

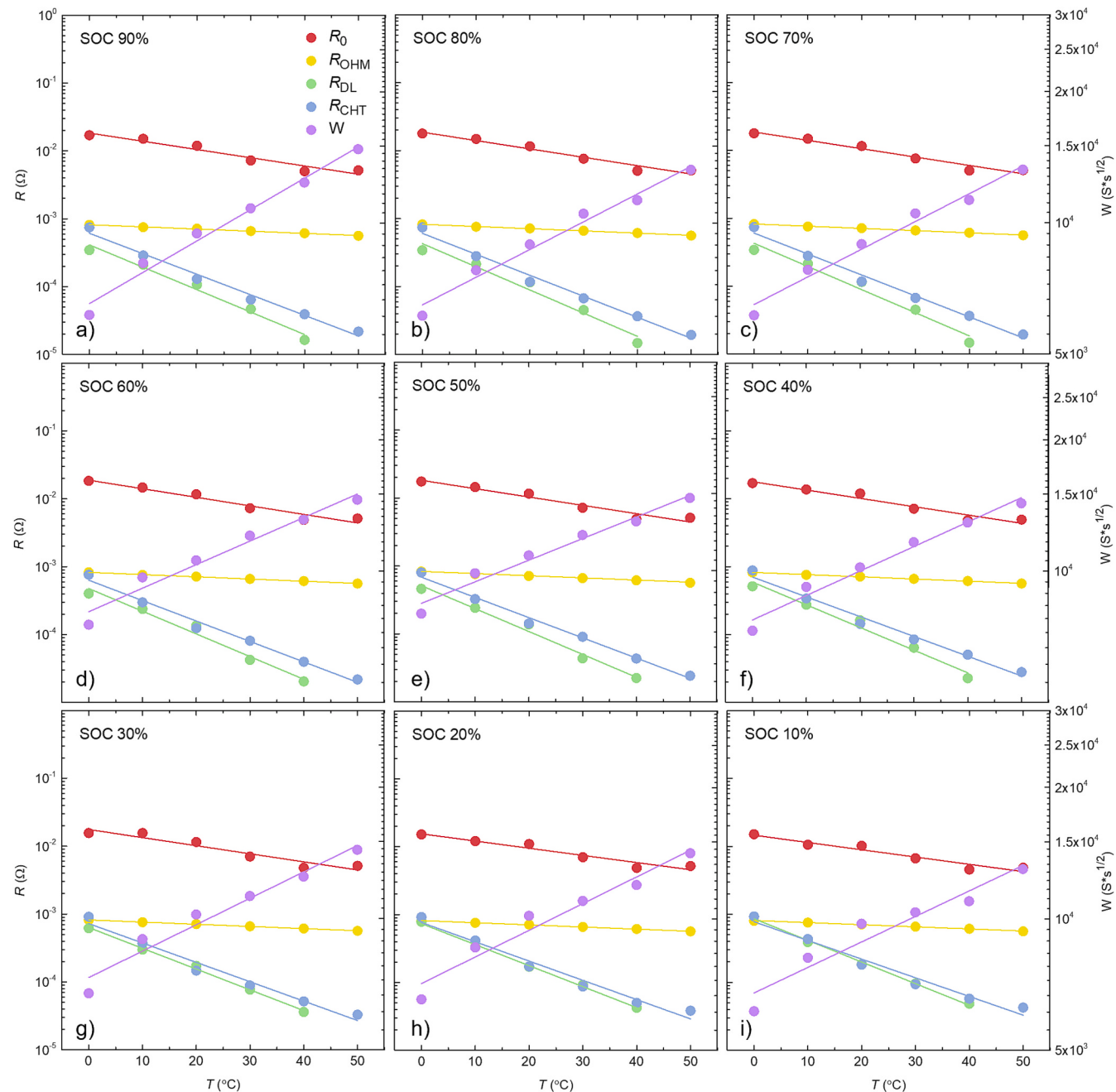


Fig. 5. Values of the fitted ECM parameters for various temperatures fitted with logarithmic functions for: (a) 90 %, (b) 80 %, (c) 70 %, (d) 60 %, (e) 50 %, (f) 40 %, (g) 30 %, (h) 20 %, and (i) 10 %.

and $\lambda = 10^{-4}$ leads to five peaks. It is evident that the choice of λ has the greatest influence on the features between $\tau = 0.1$ s and $\tau = 10$ s. From the inset in Fig. 1d it is clear that $\lambda = 10^{-4}$ is too small for the purposes of this experiment since its use leads to excessive variances in these central peaks, indicating possible over-parametrisation. On the contrary, the inset in Fig. 1c shows two central peaks with no considerable variance, making $\lambda = 10^{-3}$ the most suitable regularization parameter for calculating DRT for this system, and it will be used in this study from this point onward.

4.2. Time requirements for T_{INT} stabilisation

A series of consecutive EIS measurements was conducted at 30-min intervals at 50 °C and 0 °C (the boundary temperatures of the main experiment) to determine the time required for T_{INT} to reach and

stabilise at desired temperatures. Given that EIS measurements are highly sensitive to temperature changes, T_{INT} was considered stabilised when three consecutive Nyquist plots overlapped. Nyquist plots, for EIS measured up to 300 min after set temperatures were reached, for 50 °C and 0 °C are shown in Fig. 2a and b, respectively. From these plots, it is evident that as time increases, the Nyquist plots tend to converge until they fully overlap. At 50 °C, the Nyquist plots measured after 180 min overlap virtually completely. Similarly, at 0 °C, these plots overlap from the measurements taken after 210 min. Based on these findings, it can be concluded that T_{INT} reaches the desired temperatures with certainty after 270 min. For the purposes of the main experiment, it was decided to slightly extend this time and allow the module to relax for 5 h before further measurements.

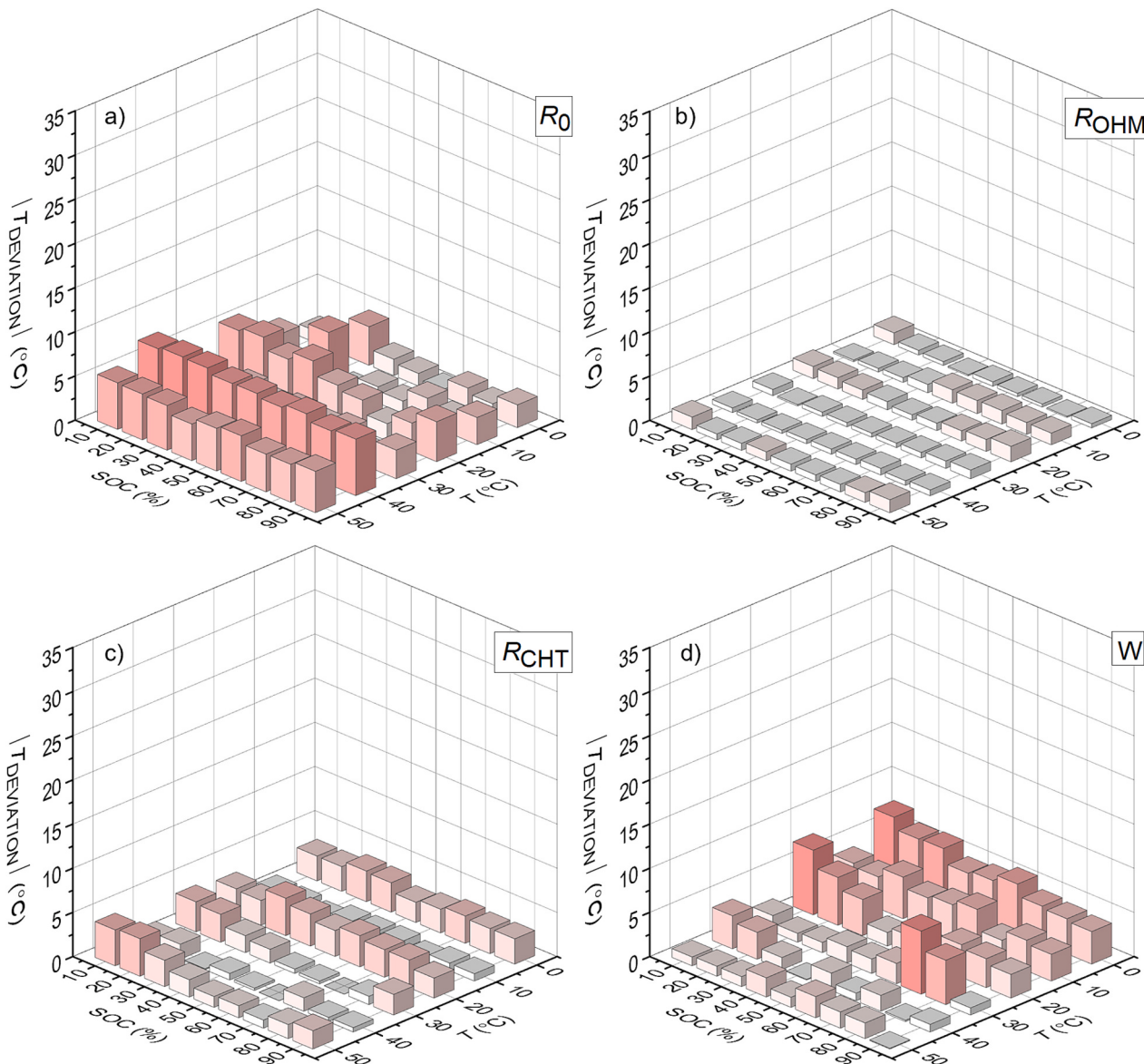


Fig. 6. Absolute deviations between the values of the fitted ECM parameters at various SOC and T and the predicted values by the fitted logarithmic functions, where (a) represents R_0 deviations, (b) R_{OHM} , (c) R_{CHT} , and (d) Warburg element deviations.

4.3. ECM at various temperatures and SOC

EIS analysis was conducted at temperatures ranging from 50 °C to 0 °C in 10 °C increments at various SOC levels, aiming to identify the most suitable ECM and DRT features for determining T_{INT} . Nyquist plots for all studied temperatures at SOC 50 % are shown in Fig. 3, while Nyquist plots for all studied temperatures at all studied SOC are available in Supplementary Materials (Fig. S1).

Here-presented Nyquist plots clearly indicate an increasing trend in both real and imaginary impedance values with decreasing temperatures. These Nyquist plots consist of an induction tail, two depressed semi-circles, and a diffusion tail. The number of these features is in agreement with the above-discussed DRT curve calculated with $\lambda = 10^{-3}$, which resulted in four easily recognizable individual peaks. The peak corresponding to low time constants (τ) can be ascribed to a high-frequency induction tail, two central peaks correspond to the two depressed semicircles, and high τ peak is associated with the low-frequency diffusion tail. Based on these observations, a suitable ECM was constructed. The schematic of this model and the individual Nyquist plot features it represents are shown in Fig. 4a.

The induction tail (occurring at the highest frequencies) is commonly attributed to the inductive properties of current collectors [47,48] and can be modelled by a single $R_0||L_0$ combination [49]. The offset of the Nyquist plot along the x-axis is ascribed to an ohmic resistance and can be modelled by a series resistor R_{OHM} . This resistance arises from the combined resistance contribution of the electrolyte, binder, separator, and current collectors [50,51].

The first depressed semicircle (corresponding to higher frequencies) is commonly ascribed to the formation and thickening of interfacial layers at the surfaces of the active anode and cathode materials. These double-layer (DL) characteristics are commonly modelled by a single $R_{\text{DL}}||\text{CPE}_{\text{DL}}$ combination. It is important to note that, due to the depressed nature of the semicircle, it is necessary to use a constant phase element (CPE) instead of the otherwise commonly used $R||C$ combination, since the usage of a simple capacitor can only model an ideal semicircle.

The second depressed semicircle (corresponding to lower frequencies) represents the charge-transfer (CHT) processes of the studied electrochemical system. These processes can be divided into partial events, describing the de-solvation of the solvated lithium ions as they

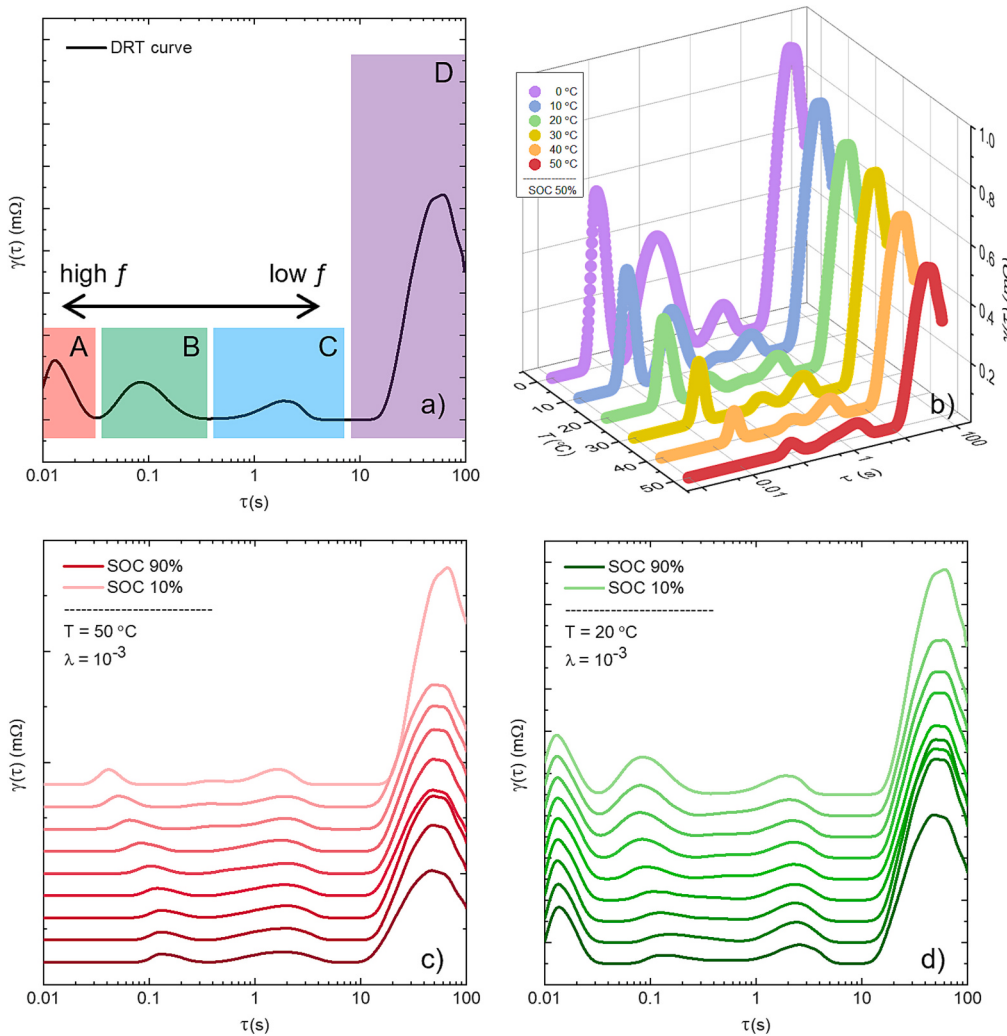


Fig. 7. (a) Visual division of a DRT curve into four peaks; (b) DRT curves for various temperatures at SOC 50 %; and DRT curves for various SOC at (c) 50 °C and (d) 20 °C.

enter the structure of the interfacial double-layer, the subsequent migration of de-solvated ions within the structure of such interfaces, and their final intercalation into the active electrode materials [52]. These processes can be modelled by another in-series connected $R_{\text{CHT}}||\text{CPE}_{\text{CHT}}$ combination.

Finally, the diffusion tail, which is the last Nyquist plot feature (representing the lowest frequencies), is used to analyse $D_{\text{Li}+}$ within the active materials and is commonly modelled by a single Warburg element (W) [53].

In order to study the temperature dependence of individual ECM elements at various SOCs, the parametrisation of all EIS data by this circuit was conducted. The results of the EIS data fitting are shown in Fig. 4b-f (the fitting was done in *Gamry Echem Analyst 2*). The values of R_0 (Fig. 4b) display low SOC dependence at temperatures of ≥ 30 °C. At lower temperatures, this dependence begins to show a trend of decreasing resistance with decreasing SOC, however, even this trend is not clear. When it comes to temperature dependence, R_0 shows a clear increase in its values with the decrease in temperatures, mainly for SOC ≥ 50 %, with the exception of the highest measured temperature of 50 °C, when R_0 shows almost identical values as R_0 for 40 °C. This finding suggests that this parameter is not suitable for determining T_{INT} , as it would struggle to distinguish between temperatures above 40 °C, which would hinder its use in any real-world application. The ohmic resistance R_{OHM} (Fig. 4c) shows almost non-existent SOC dependency. In contrast, however, R_{OHM} displays a nearly incremental temperature

dependency. These findings suggest that this parameter could be suitable candidate for determining T_{INT} , even without a need to know the value of SOC at which T_{INT} is measured. Resistance of the double-layer interfaces R_{DL} (Fig. 4d) shows low SOC dependency at temperatures of ≥ 20 °C and a seemingly gradual increase in resistance with decreasing temperature. The semicircle ascribed to R_{DL} , however, decreases with increasing temperature, and at 50 °C, this semicircle disappears completely. The origin of such disappearance lies in the temperature-elevated kinetic properties of the double layer interfaces. At some point under elevated temperatures, their impedance response becomes so low that it is completely overshadowed by other impedance contributors. This suggests that the impedance contribution of processes ascribed to R_{DL} is entirely overshadowed by charge-transfer processes. The inability to detect and study this feature at 50 °C makes R_{DL} unsuitable for determining T_{INT} at elevated temperatures. Charge-transfer resistance R_{CHT} (Fig. 4e) increases with decreasing SOC, while these changes are more pronounced at lower temperatures. Values of Warburg elements (Fig. 4f) describe the development of the combined diffusivity of lithium ions in the active cathode and anode materials as a function of SOC. In terms of temperature dependency, a clear trend of increasing values of Warburg element with rising temperature is observed. To study the relationship between individual ECM elements and temperature at various SOCs, Fig. 5 was constructed. ECM values obtained earlier via EIS data fitting were plotted as a function of temperature, while these data were fitted by logarithmic functions to model the temperature

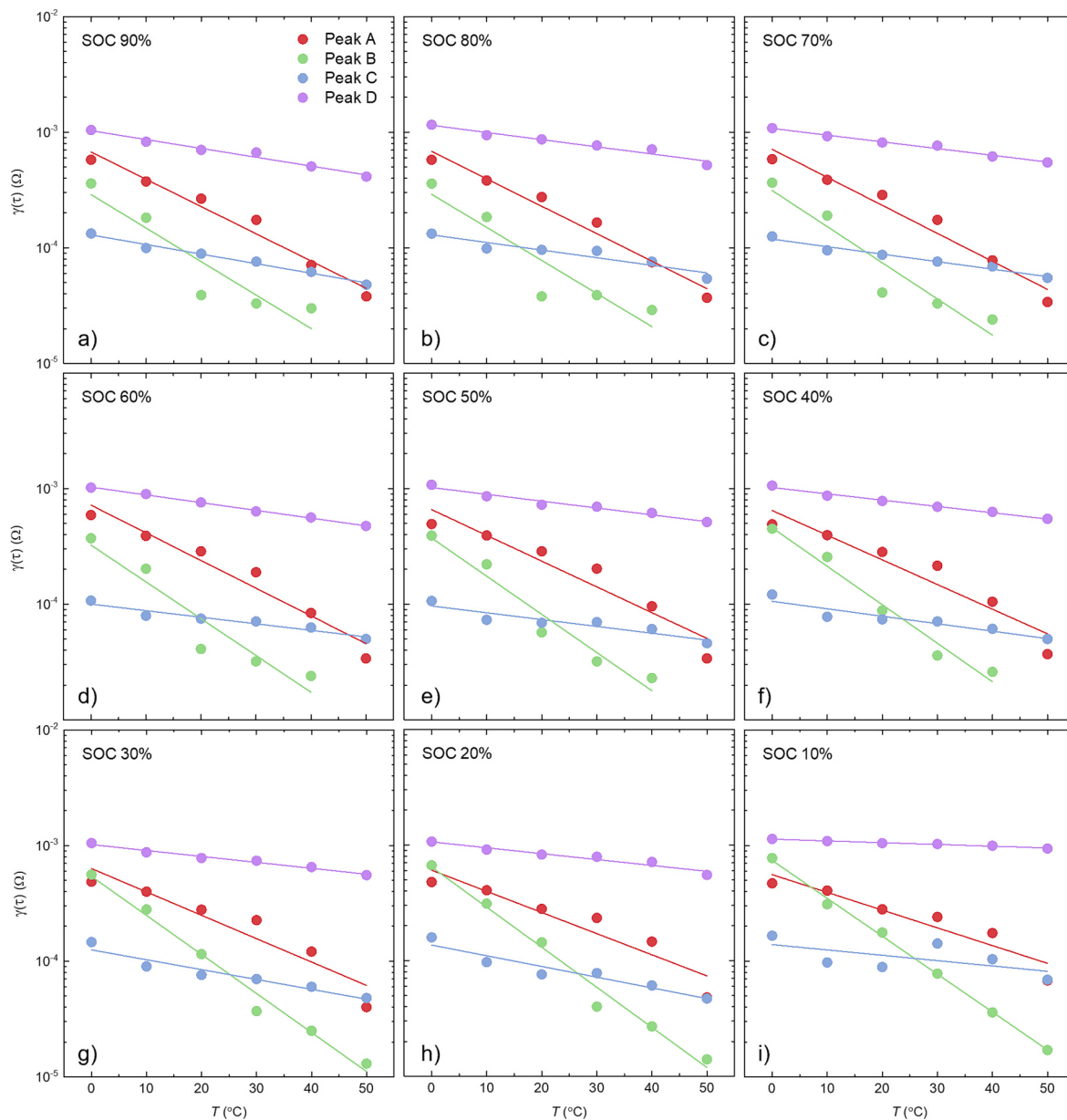


Fig. 8. Maximum values of individual DRT peaks for various temperatures fitted with logarithmic functions for: (a) 90 %, (b) 80 %, (c) 70 %, (d) 60 %, (e) 50 %, (f) 40 %, (g) 30 %, (h) 20 %, and (i) 10 %.

dependent behaviour of individual elements.

Subsequently, the absolute deviation ($|T_{DEV}|$) between the fitted ECM elements and the modelled functions was calculated and plotted in Fig. 6. R_{DL} was not considered for this analysis due to the disappearance of the $R_{DL}||CPE_{DL}$ feature in Nyquist plots obtained at 50 °C, as this disappearance clearly renders R_{DL} unsuitable for the here-discussed purposes.

The maximum temperature deviations, $|T_{DEV, R_0, MAX}| = 7.46$ °C and $|T_{DEV, W, MAX}| = 7.21$ °C, can be considered too high for satisfactorily accurate determination of T_{INT} , suggesting that R_0 and W are also unsuitable for such purposes. In contrast, R_{OHM} and R_{CHT} led to maximum deviations values of $|T_{DEV, R_{OHM}, MAX}| = 1.75$ °C and $|T_{DEV, R_{CHT}, MAX}| = 4.26$ °C, indicating that the determination of T_{INT} via R_{OHM} and R_{CHT} is viable. However, it is important to note that both R_{OHM} and R_{CHT} are parameters whose values can be strongly affected by various degradation processes. The ohmic resistance of the battery module can significantly increase, for instance, due to the cyclic degradation of the electrolyte. The resistance associated with charge-transfer processes is

highly sensitive to degradation events that result in a loss of lithium inventory, such as particle cracking or the development of SEI layer [54,55]. Taking this into account, the use of R_{OHM} and R_{CHT} for reliable determination of T_{INT} of battery modules would require a complex matrix of these ECM elements obtained at various temperatures and states of charge for modules that have undergone a wide range of various degradation processes. Considering these arguments, it is desirable to explore alternative approaches for determining T_{INT} .

4.4. DRT at various temperatures and SOC

As it was mentioned in the previous chapter, the DRT curve consists of several peaks that can be attributed to electrochemical processes or features of the corresponding Nyquist plot. A visual representation of the DRT curve, highlighting the individual recognizable peaks, is provided in Fig. 7a.

Peak A can be attributed to the processes related to the electric/electromagnetic properties of current collectors (parallel to $R_0||L_0$)

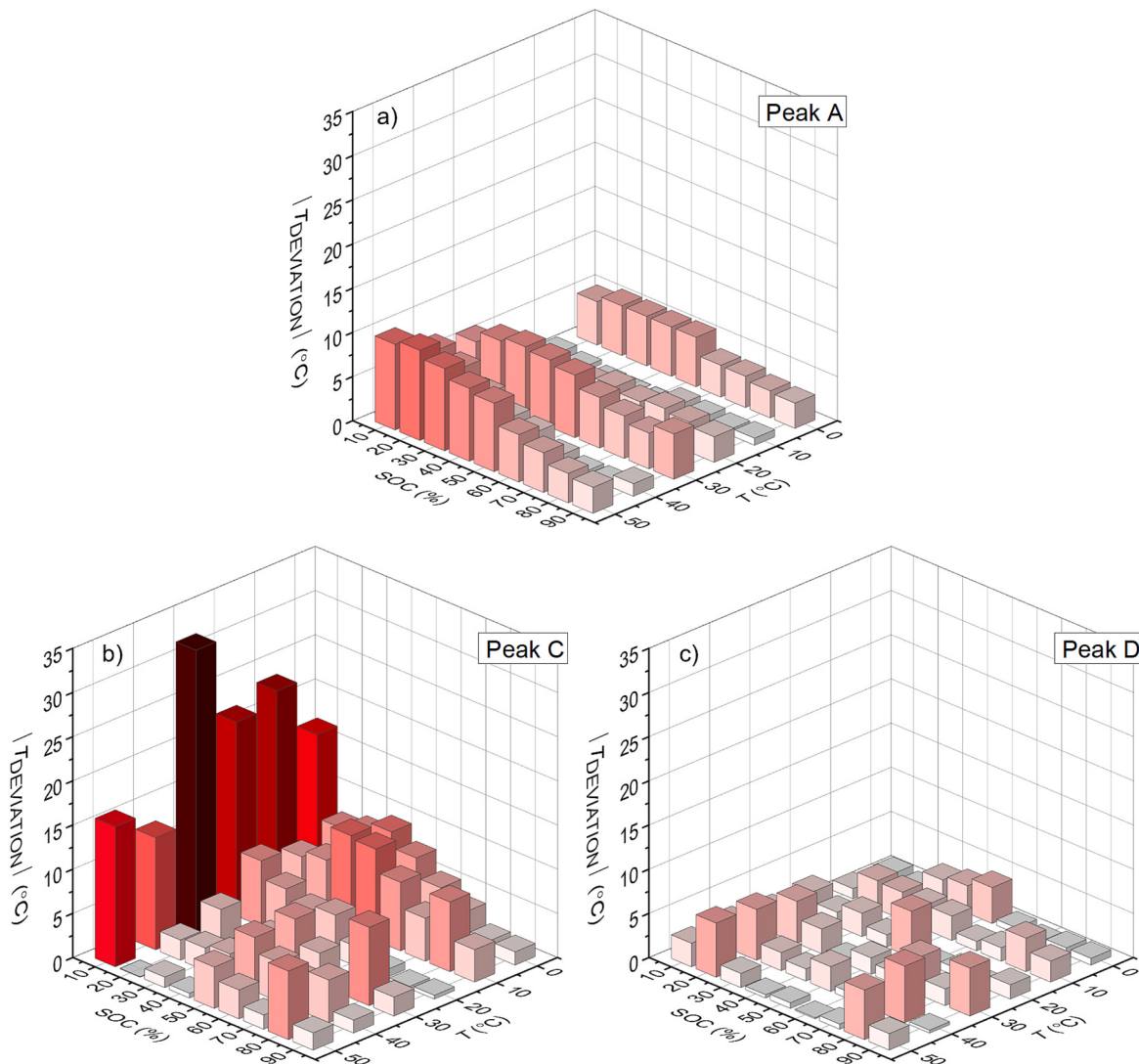


Fig. 9. Absolute deviations between the measured maxima values of individual DRT peaks at various SOC and T and the predicted values by the fitted logarithmic functions, where (a) represents Peak A, (b) Peak C, and (c) Peak D deviations.

combination in used ECM), Peak B describes the properties of double-layers (parallel to $R_{DL}||CPE_{DL}$), Peak C follows the charge-transfer features (parallel to $R_{CHT}||CPE_{CHT}$), and Peak D is ascribed to the processes related to the diffusion of lithium ions (parallel to Warburg element). The DRT curves were calculated by standard Tikhonov regularization using $\lambda = 10^{-3}$ for all measured EIS data. The DRT curves for all studied temperatures at SOC 50 % are shown in Fig. 7b. From this plot, it is evident that all DRT peaks increase in magnitude with decreasing temperatures, while there are also observable shifts in the time constants at which these peaks are manifested, particularly for Peak A. Fig. 7c and d display DRT curves for all studied SOC levels at 50 °C and 20 °C, respectively. At 20 °C, the magnitude of Peak B increases with decreasing SOC. At 50 °C however, Peak B for SOC $\geq 40\%$ disappears, indicating that Peak B (similarly to R_{DL}) is not suitable for determining T_{INT} (this disappearance is highlighted in Fig. S2).

As shown in Fig. 8, the changes in magnitudes of all DRT peaks across the temperatures and SOC levels were collected and fitted by logarithmic functions, in order to study the ability of DRT peaks to determine T_{INT} . From visual analysis, it is clear that Peak B, aside from SOC $\leq 30\%$, lacks consistency in providing a usable trend for determining T_{INT} . To evaluate the ability of the remaining peaks to determine T_{INT} , the absolute deviations between the magnitudes of individual DRT peaks and the fitted logarithmic functions were calculated (Fig. 9). Peak A at SOC

above 50 % shows a great ability to determine the temperature with $|T_{DEV, Peak A, MAX}| \leq 6$ °C. However, at lower SOCs, the deviation increases up to 10 °C, making it insufficient for accurate temperature estimation in the SOC $\leq 50\%$ region (Fig. 9a). Peak C suffers from insufficient accuracy across the range of studied SOCs and temperatures (particularly at lower SOCs and lower temperatures), rendering it unsuitable for temperature determination (Fig. 9b). Peak D, on the other hand, shows $|T_{DEV, Peak D}| \leq 6$ °C across all SOC levels, indicating its potential for accurate T_{INT} determination.

When comparing the ability of Peak A and Peak D to determine T_{INT} , Peak D outperforms Peak A by providing desired accuracy for the entire SOC range, whereas Peak A achieves such accuracy only for SOCs above 50 %.

However, it is important to note that Peak A is calculated from the high-frequency region of the EIS spectra which can be obtained within the tens of seconds, while Peak D is calculated from the low-frequency region of the EIS spectra, and obtaining such data can take several tens of minutes. This makes the acquisition of the EIS data for the calculation of Peak D highly time-consuming. Moreover, EIS is generally measured during a non-operational state of the battery, and in such cases, tens of minutes of non-operation may allow the module to change its temperature significantly, potentially resulting in false temperature estimation. For instance, if the module cools down during this period,

the subsequent estimation might falsely indicate lower T_{INT} , which, in extreme situations, could have hazardous consequences. Furthermore, this low-frequency peak is associated with D_{Li+} processes, where degradation events originating in structural changes of active materials may influence the magnitude of this peak. Given these drawbacks, the implementation of Peak D for estimating T_{INT} in real-world applications is highly problematic.

Peak A, however, can be obtained in under a minute, thus, this feature does not suffer from time-induced deviations. Also, this high-frequency peak is associated with electric/electromagnetic properties of Al and Cu current collectors, where even unlikely corrosion of such metal sheets is expected to have only insignificant effect on such properties. Taking all these factors into account, Peak A emerges as the single suitable DRT feature for determining T_{INT} in the studied battery module, provided the SOC remains above 50 %.

5. Conclusion

This study offers insight into the potential of EIS and DRT features for determining the internal temperature of EV battery modules, both for EV and 2nd life applications. The EV module was subjected to temperatures ranging from 0 °C to 50 °C in 10 °C increments. At each temperature step, EIS measurements were conducted across various states of charge ranging from SOC 10 % to SOC 90 % in 10 % increments. These EIS data were analysed using ECM and DRT methods, and their ability to determine T_{INT} was thoroughly evaluated.

Regarding the ECM parameters, R_0 , R_{DL} and W were found unsuitable for temperature determination in the studied module. In contrast, R_{CHT} , and, particularly, R_{OHM} provided adequate accuracies, however, given that these two parameters are highly sensitive to degradation events, a comprehensive dataset of batteries that have experienced various degradation scenarios is necessary. This complexity makes their application in real-world conditions highly problematic.

In the case of DRT, four distinct peaks were identified. Peak B and Peak C were deemed unsuitable. On the contrary, Peak A (for SOCs above 50 %) and Peak D (across the entire SOC range) led to promising results for temperature determination. Despite this, Peak D suffers from two disadvantages: I. Its magnitude is related to the diffusion of lithium ions, and hence, it may vary significantly with structural changes of active materials. II. The acquisition of the EIS data for the calculation of Peak D is highly time-consuming, hindering its use for on-board applications. Moreover, the extended measurements may allow the battery to drift from its original temperature, leading to inaccuracies in temperature determination. On the other hand, Peak A is associated with the electric/electromagnetic properties of the current collectors. Since commercial current collectors in conventional Li-ion batteries are typically Al sheets for cathodes and Cu sheets for anodes, it is expected that their electric/electromagnetic behaviour will remain consistent across standard Li-ion batteries. Therefore, Peak A can be regarded as reliable candidate for determining the internal temperature. Furthermore, even if the unlikely corrosion of current collectors occurs, its impact on the electric/electromagnetic properties of such metal sheets is assumed to be minimal, making Peak A suitable even for scenarios with elevated degradation.

The findings and discussions in this work lead to the conclusion that, among all ECM and DRT features, the high-frequency DRT Peak A is the most suitable feature for determining the internal temperature in EV battery modules, both in EV and 2nd life applications.

CRediT authorship contribution statement

M. Kemeny: Writing – original draft, Visualization, Methodology, Investigation, Formal analysis, Conceptualization. **P. Ondrejka:** Writing – review & editing, Conceptualization. **D. Sismisova:** Resources, Funding acquisition. **M. Mikolasek:** Supervision, Resources, Project administration, Conceptualization.

Declaration of competing interest

The authors declare that they have no known competing financial interests or personal relationships that could have appeared to influence the work reported in this paper.

Acknowledgements

This work was supported by the grants VEGA 1/0707/24, APVV-22-0132 and APVV-20-0111. Moreover, this work was supported within the Operational Programme Integrated Infrastructure for the project: Regeneration of used batteries from electric vehicles, ITMS2014+: 313012BUN5, which is part of the Important Project of Common European Interest (IPCEI), called European Battery Innovation in the Operational Program Integrated Infrastructure, call code: OPII-MH/DP/2021/9.5-34, co-financed from the resources of the European Regional Development Fund.

Appendix A. Supplementary data

Supplementary data to this article can be found online at <https://doi.org/10.1016/j.est.2024.114566>.

Data availability

Data will be made available on request.

References

- [1] Erika Teliz, Carlos F. Zinola, Verónica Diaz, Identification and quantification of ageing mechanisms in Li-ion batteries by electrochemical impedance spectroscopy, *Electrochim. Acta* 426 (2022) 140801.
- [2] Yaosen Tian, et al., Promises and challenges of next-generation “beyond Li-ion” batteries for electric vehicles and grid decarbonization, *Chem. Rev.* 121 (3) (2020) 1623–1669.
- [3] Jianping Wen, Dan Zhao, Chuanwei Zhang, An overview of electricity powered vehicles: Lithium-ion battery energy storage density and energy conversion efficiency, *Renew. Energy* 162 (2020) 1629–1648.
- [4] Henok Ayele Behabtu, et al., A review of energy storage technologies’ application potentials in renewable energy sources grid integration, *Sustainability* 12 (24) (2020) 10511.
- [5] Kudakwashe Chayambuka, et al., From li-ion batteries toward Na-ion chemistries: challenges and opportunities, *Adv. Energy Mater.* 10 (38) (2020) 2001310.
- [6] Reiner Korthauer (Ed.), *Lithium-ion Batteries: Basics and Applications*, Springer, 2018.
- [7] Yuanli Ding, et al., Automotive Li-ion batteries: current status and future perspectives, *Electrochim. Energy Rev.* 2 (2019) 1–28.
- [8] Weldjewergis Gebrewahid Kidanu, et al., High capacity and inexpensive multivalent cathode materials for aqueous rechargeable Zn-ion battery fabricated via *in situ* electrochemical oxidation of VO₂ nanorods, *J. Power Sources* 523 (2022) 231060.
- [9] Pius Victor Chombo, Yossapong Laoonual, A review of safety strategies of a Li-ion battery, *J. Power Sources* 478 (2020) 228649.
- [10] Bin Xu, et al., Mitigation strategies for Li-ion battery thermal runaway: a review, *Renew. Sustain. Energy Rev.* 150 (2021) 111437.
- [11] Ganghui Zeng, et al., Thermal safety study of Li-ion batteries under limited overcharge abuse based on coupled electrochemical-thermal model, *Int. J. Energy Res.* 44 (5) (2020) 3607–3625.
- [12] Zhenpo Wang, et al., Overcharge-to-thermal-runaway behavior and safety assessment of commercial lithium-ion cells with different cathode materials: a comparison study. *Journal of energy, Chemistry* 55 (2021) 484–498.
- [13] Shuai Ma, et al., Temperature effect and thermal impact in lithium-ion batteries: a review, *Prog. Nat. Sci.: Mater. Int.* 28 (6) (2018) 653–666.
- [14] Jacqueline S. Edge, et al., Lithium ion battery degradation: what you need to know, *Phys. Chem. Chem. Phys.* 23 (14) (2021) 8200–8221.
- [15] Depeng Kong, et al., A review of early warning methods of thermal runaway of lithium ion batteries, *J. Energy Storage* 64 (2023) 107073.
- [16] Xi Zhang, et al., A critical review of thermal runaway prediction and early-warning methods for lithium-ion batteries. *Energy material, Advances* 4 (2023) 0008.
- [17] T.M.M. Heenan, et al., Mapping internal temperatures during high-rate battery applications, *Nature* 617 (7961) (2023) 507–512.
- [18] L.H.J. Rajmakers, et al., A review on various temperature-indication methods for Li-ion batteries, *Appl. Energy* 240 (2019) 918–945.
- [19] Henrik Beelen, et al., Towards impedance-based temperature estimation for Li-ion battery packs, *Int. J. Energy Res.* 44 (4) (2020) 2889–2908.
- [20] Micael Nascimento, et al., Internal strain and temperature discrimination with optical fiber hybrid sensors in Li-ion batteries, *J. Power Sources* 410 (2019) 1–9.

- [21] Kieran Mc carthy, et al., Use of impedance spectroscopy for the estimation of Li-ion battery state of charge, state of health and internal temperature, *J. Electrochem. Soc.* 168 (8) (2021) 080517.
- [22] Jaya Yadav, et al., Reinforcing Li-ion Batteries with Electrochemical Impedance Spectroscopy, *Proceedings, Materials Today*, 2023.
- [23] A.G. Li, W. Wang, A.C. West, M. Preindl, Health and performance diagnostics in Li-ion batteries with pulse-injection-aided machine learning, *Appl. Energy* 315 (2022) 119005.
- [24] J. Tian, R. Xiong, C. Chen, C. Wang, W. Shen, F. Sun, Simultaneous prediction of impedance spectra and state for lithium-ion batteries from short-term pulses, *Electrochim. Acta* 449 (2023) 142218.
- [25] Miriam Steinhauer, et al., Investigation of the solid electrolyte interphase formation at graphite anodes in lithium-ion batteries with electrochemical impedance spectroscopy, *Electrochim. Acta* 228 (2017) 652–658.
- [26] Samuel Cruz-manzo, Paul Greenwood, An impedance model based on a transmission line circuit and a frequency dispersion Warburg component for the study of EIS in Li-ion batteries, *J. Electroanal. Chem.* 871 (2020) 114305.
- [27] Yige Li, et al., State-of-health prediction for lithium-ion batteries via electrochemical impedance spectroscopy and artificial neural networks, *Energy Storage* 2 (5) (2020) e186.
- [28] Nina Meddings, et al., Application of electrochemical impedance spectroscopy to commercial Li-ion cells: a review, *J. Power Sources* 480 (2020) 228742.
- [29] Laurence A. Middlemiss, et al., Characterisation of batteries by electrochemical impedance spectroscopy, *Energy Rep.* 6 (2020) 232–241.
- [30] Maximilian Bruch, et al., Novel method for the parameterization of a reliable equivalent circuit model for the precise simulation of a battery cell's electric behavior, *J. Power Sources* 490 (2021) 229513.
- [31] Pietro Iurilli, Claudio Brivio, Vanessa Wood, On the use of electrochemical impedance spectroscopy to characterize and model the aging phenomena of lithium-ion batteries: a critical review, *J. Power Sources* 505 (2021) 229860.
- [32] Mohammed A. Zabara, et al., Insights into charge transfer dynamics of Li batteries through temperature-dependent electrochemical impedance spectroscopy (EIS) utilizing symmetric cell configuration, *Electrochim. Acta* 485 (2024) 144080.
- [33] Simone Barcellona, et al., Aging effect on the variation of Li-ion battery resistance as function of temperature and state of charge, *J. Energy Storage* 50 (2022) 104658.
- [34] Rong He, et al., Comparative analysis for commercial li-ion batteries degradation using the distribution of relaxation time method based on electrochemical impedance spectroscopy, *Energy* 263 (2023) 125972.
- [35] Min Jae Jung, Sang-Gug Lee, Kyung-Sik Choi, A new diagnostic indicator for lithium-ion batteries via electrochemical impedance spectroscopy: harnessing the highest frequency peak in distribution of relaxation times, *J. Power Sources* 611 (2024) 234743.
- [36] Davide Clematis, et al., On the stabilization and extension of the distribution of relaxation times analysis, *Electrochim. Acta* 391 (2021) 138916.
- [37] Roby Soni, et al., Lithium-sulfur battery diagnostics through distribution of relaxation times analysis, *Energy Storage Mater.* 51 (2022) 97–107.
- [38] Rong He, et al., Comparative analysis for commercial li-ion batteries degradation using the distribution of relaxation time method based on electrochemical impedance spectroscopy, *Energy* 263 (2023) 125972.
- [39] Leo Wildfeuer, Philipp Gieler, Alexander Karger, Combining the distribution of relaxation times from EIS and time-domain data for parameterizing equivalent circuit models of lithium-ion batteries, *Batteries* 7 (3) (2021) 52.
- [40] Tobias G. Bergmann, Nicolas Schlüter, Introducing alternative algorithms for the determination of the distribution of relaxation times, *ChemPhysChem* 23 (13) (2022) e202200012.
- [41] Michael A. Danzer, Generalized distribution of relaxation times analysis for the characterization of impedance spectra, *Batteries* 5 (3) (2019) 53.
- [42] K.T. Malkow, A theory of distribution functions of relaxation times for the deconvolution of immittance data, *J. Electroanal. Chem.* 838 (2019) 221–231.
- [43] A.L. Gavriluk, D.A. Osinkin, D.I. Bronin, On a variation of the Tikhonov regularization method for calculating the distribution function of relaxation times in impedance spectroscopy, *Electrochim. Acta* 354 (2020) 136683.
- [44] A.L. Gavriluk, D.A. Osinkin, D.I. Bronin, The use of Tikhonov regularization method for calculating the distribution function of relaxation times in impedance spectroscopy, *Russ. J. Electrochem.* 53 (2017) 575–588.
- [45] Nicolas Schlüter, Sabine Ernst, Uwe Schröder, Finding the optimal regularization parameter in distribution of relaxation times analysis, *ChemElectroChem* 6 (24) (2019) 6027–6037.
- [46] Wei Gao, et al., Evaluation of the second-life potential of the first-generation Nissan leaf battery packs in energy storage systems, *eTransportation* 20 (2024) 100313.
- [47] Lisa Deleebecq, Sune Veltzé, Electrochemical impedance spectroscopy study of commercial Li-ion phosphate batteries: a metrology perspective, *Int. J. Energy Res.* 44 (9) (2020) 7158–7182.
- [48] Yoshitaka Inui, Satoshi Hirayama, Tadashi Tanaka, Investigation of time domain measurement of electrochemical impedance spectrum in low frequency range for lithium-ion batteries using preset equivalent circuit model, *J. Electroanal. Chem.* 950 (2023) 117894.
- [49] Ji'ang Zhang, et al., Variable-order equivalent circuit modeling and state of charge estimation of lithium-ion battery based on electrochemical impedance spectroscopy, *Energies* 14 (3) (2021) 769.
- [50] Jaya Yadav, et al., Reinforcing Li-Ion Batteries with Electrochemical Impedance Spectroscopy, *Proceedings, Materials Today*, 2023.
- [51] Yanshuo Liu, et al., State-of-health estimation of lithium-ion batteries based on electrochemical impedance spectroscopy: a review. *Protection and control of, Modern Power Syst.* 8 (3) (2023) 1–17.
- [52] T. Richard Jow, et al., Factors limiting Li+ charge transfer kinetics in Li-ion batteries, *J. Electrochem. Soc.* 165 (2) (2018) A361.
- [53] Woosung Choi, et al., Modeling and applications of electrochemical impedance spectroscopy (EIS) for lithium-ion batteries. *Journal of electrochemical, Sci. Technol.* 11 (1) (2020) 1–13.
- [54] Carlos Pastor-Fernández, et al., Identification and quantification of ageing mechanisms in Lithium-ion batteries using the EIS technique, in: 2016 IEEE Transportation Electrification Conference and Expo (ITEC), IEEE, 2016, pp. 1–6.
- [55] Jiangong Zhu, et al., Investigation of lithium-ion battery degradation mechanisms by combining differential voltage analysis and alternating current impedance, *J. Power Sources* 448 (2020) 227575.